

Bridging Scales in Black Hole Accretion and Feedback: Subgrid Prescription from First Principles

HYERIN CHO (조혜린),^{1, 2} BEN S. PRATHER,^{1, 2} RAMESH NARAYAN,^{1, 2} KUNG-YI SU,^{3, 1, 2} ANGELO RICARTE,^{1, 2} PRIYAMVADA NATARAJAN,^{2, 4, 5} AND ANTONIO J. PORRAS-VALVERDE⁴

¹Center for Astrophysics | Harvard & Smithsonian, 60 Garden Street, Cambridge, MA 02138, USA

²Black Hole Initiative at Harvard University, 20 Garden Street, Cambridge, MA 02138, USA

³Department of Physics & Astronomy and Center for Interdisciplinary Exploration and Research in Astrophysics(CIERA), Northwestern University, 1800 Sherman Ave, Evanston, IL 60201, USA

⁴Department of Astronomy, Yale University, Kline Tower, 266 Whitney Avenue, New Haven, CT 06511, USA

⁵Department of Physics, Yale University, P.O. Box 208121, New Haven, CT 06520, USA

ABSTRACT

Understanding how supermassive black holes (BHs) couple to their host galaxies across a vast spatial and temporal dynamic range remains a central challenge in galaxy evolution. Using the multizone framework—designed to capture bidirectional inflow–outflow from the event horizon to the Bondi scale—we present a suite of long-duration GRMHD simulations spanning BH spins $|a_*| = 0\text{--}0.9$ and Bondi radii $R_B/r_g = 4 \times 10^2\text{--}2 \times 10^6$. From these simulations we derive spin-dependent subgrid prescriptions from first principles, applicable to hot accretion flows with low-Eddington ratios ($f_{\text{Edd}} \lesssim 10^{-3}$), for adoption in cosmological simulations and semi-analytic models. We provide compact analytic fits for the time-averaged accretion rate $\dot{M}(R_B, a_*)$ and feedback power $\dot{E}_{\text{fb}}(R_B, a_*)$ with respect to the Bondi rate \dot{M}_B , which are largely insensitive to the initial gas configuration and magnetic field strength. To capture intrinsic time-variability, we also quantify the full distributions of \dot{M} and feedback efficiency η , both well described by lognormal statistics, with widths that increase toward larger R_B . We further measure self-consistent spin evolution in the hot accretion mode, finding that the spinup parameter varies as $s(a_*) \simeq -3.7a_*$, which implies a very long spindown timescale $t_s \simeq 12(10^{-3}/f_{\text{Edd}})$ Gyr. Thus, BH spins are effectively frozen during phases of quiescent accretion. Compared to conventional small-domain GRMHD calculations, our simulations, which reach dynamical equilibrium across horizon-to-galaxy scales, yield systematically different long-term accretion, feedback, and spin properties, cautioning against direct extrapolation from small-scale GRMHD simulations when constructing galactic-scale subgrid models.

Keywords: Accretion (14), Active galactic nuclei (16), Bondi accretion (174), Kerr black holes (886), Relativistic jets (1390), Supermassive black holes (1663), Magnetohydrodynamical simulations (1966)

1. INTRODUCTION

Supermassive black holes (BHs) at the centers of massive galaxies are thought to co-evolve with their hosts (see e.g., Natarajan 2011; Kormendy & Ho 2013; Heckman & Best 2014, for reviews). Galaxies supply gas for BH accretion, while BHs return energy and momentum via feedback, establishing an accretion–feedback loop that can quench star formation in massive “red and dead” systems. At low Eddington ratios, typical of many nearby supermassive BHs, accretion proceeds through hot, radiatively inefficient, advection dominated accretion flows (ADAFs; see Yuan & Narayan 2014, for a review). In this regime, an important feedback channel

is the Blandford & Znajek (1977) mechanism, in which magnetic fields threading a spinning BH launch relativistic jets that extract the BH’s rotational energy, a magnetic-field analogue of the Penrose (1969) process (Komissarov 2009; Lasota et al. 2014).

The BH–galaxy coupling spans an enormous range of scales. In M87, a Schwarzschild radius of ~ 0.6 mpc connects to jet emission observed from tens of Schwarzschild radii (Lu et al. 2023; EHT MWL Science Working Group et al. 2021) out to ~ 20 kpc radio lobes (Owen et al. 2000). Capturing such two-way coupling poses a major computational challenge. Horizon-scale GRMHD simulations (e.g., Komissarov 1999; Gammie et al. 2003;

Sadowski et al. 2013; White et al. 2016; Porth et al. 2019; Liska et al. 2022; Prather 2024) self-consistently resolve accretion and jet launching but typically achieve steady states only out to \lesssim a few hundred horizon radii. By contrast, cosmological and galaxy simulations (e.g., Tremmel et al. 2017; Weinberger et al. 2018; Davé et al. 2019; Ni et al. 2022; Wellons et al. 2023; Schaye et al. 2025) require subgrid prescriptions for unresolved BH accretion and feedback. Zoom-in/hyper-refinement approaches, which begin with coarse resolution and progressively enhance it (e.g., Hopkins & Quataert 2010; Ressler et al. 2020; Anglés-Alcázar et al. 2021; Guo et al. 2023, 2024; Hopkins et al. 2024a,b, 2025; Kaaz et al. 2025), can track inflow from galactic to BH scales, but still struggle to propagate feedback back to the galaxy.

A key uncertainty in cosmological simulations is therefore the BH subgrid model: differing implementations produce a wide range of predictions (e.g., Habouzit et al. 2022; Haidar et al. 2022; Weinberger et al. 2023; Wellons et al. 2023). Some physically-motivated approaches adopt highly idealized analytic prescriptions for accretion (e.g., Bondi 1952; Shakura & Sunyaev 1973; Novikov & Thorne 1973; Narayan & Yi 1994) and feedback (e.g., Blandford & Znajek 1977), or incorporate spin-dependent feedback (Dubois et al. 2021; Talbot et al. 2021; Beckmann et al. 2025; Huško et al. 2025) calibrated on small-domain GRMHD calculations (Tchekhovskoy et al. 2012; McKinney et al. 2012; Ricarte et al. 2023; Lowell et al. 2024). However, how reliably small-scale GRMHD results carry over to galactic scales remains largely untested.

The “multizone method” developed by our group bridges this gap, enabling first-principles GRMHD simulations that connect the horizon to beyond the Bondi radius across \sim 8 orders of magnitude (Cho et al. 2023, 2024, 2025; Su et al. 2025a). Subsequently, similar scale-bridging methods have since been implemented for Cartesian grids (Guo et al. 2025) and for Lagrangian simulations (Hopkins & Most 2025).

For non-spinning BHs, Cho et al. (2023, 2024) showed that magnetic fields strongly suppress \dot{M} relative to the Bondi prediction \dot{M}_B (Bondi 1952), with the suppression depending on the Bondi radius R_B (defined in Equation 1). Long evolutions reach the magnetically arrested disk (MAD) state (Narayan et al. 2003; Igumenshchev et al. 2003, see also Bisnovatyi-Kogan & Ruzmaikin 1974, 1976), where saturated magnetic flux drives highly non-axisymmetric inflow via interchange instabilities. Magnetic fields also strongly brake rotation, effectively erasing memory of the initial gas angular momentum (Cho et al. 2024). For spinning BHs ($a_* = 0.9$), Cho et al. (2025) found a time-averaged

feedback efficiency $\eta \approx 0.3$ (defined in Equation 4) independent of R_B and regardless of the initial gas rotation state. The insensitivity of the final state to the initial gas rotation is consistent with Cho & Narayan (2025)’s predictions that systems eventually evolve to a strongly variable state, characterized by flips in rotation and large jet-power fluctuations (e.g., Ressler et al. 2021; Kwan et al. 2023; Lalakos et al. 2024; Cho et al. 2024, 2025; Galishnikova et al. 2025; Kim & Most 2025; Guo et al. 2025; Chan et al. 2025; Lalakos et al. 2025). Some of the early multizone results have already begun to be incorporated into galaxy simulations (Su et al. 2025a), cosmological simulations (Su et al. 2025b), and semi-analytic models (SAMs) (Porras-Valverde et al. 2025).

In this work, we extend the multizone method to a grid of BH spins, $a_* = 0, 0.1, 0.3, 0.5, 0.7, 0.9$, and explore the dependence on R_B at each spin. From this library, we derive simple subgrid prescriptions for the time-averaged BH accretion rate \dot{M} and feedback power \dot{E}_{fb} that are obtained directly from large-scale, first-principles GRMHD simulations. They are not tuned to observations, and are straightforward to implement in cosmological simulations and SAMs. We describe the numerical method in Section 2, present the subgrid prescriptions in Section 3, outline spin evolution in Section 4, and conclude in Section 5.

Throughout this work, we adopt units where $GM = c = 1$, so our units of length and time are the gravitational radius $r_g \equiv GM/c^2$ and the gravitational time $t_g \equiv r_g/c$. Although our GRMHD simulations are scale-free and are, in principle, applicable to any BH mass M , we focus on supermassive BHs in galactic centers. We define the Bondi radius as

$$R_B \equiv \frac{GM}{c_{s,\infty}^2} \approx \frac{7 \times 10^{12} \text{ K}}{\gamma_{\text{ad}} T_{\infty}} r_g, \quad (1)$$

where $c_{s,\infty}$ and T_{∞} are the sound speed and temperature (in K) of the gas outside the Bondi radius. We use an adiabatic index $\gamma_{\text{ad}} = 5/3$. The Bondi timescale t_B is defined as the free-fall timescale measured at the Bondi radius: $t_B \equiv (R_B/r_g)^{3/2} t_g$.

The low Eddington-ratio accretion flows we study in this work typically consist of hot coronal gas from the galaxy flowing in at the Bondi radius and accreting on the supermassive BH. The temperature T_{∞} in Equation 1 is then of order the virial temperature of the galaxy, which is $T_{\infty} \sim 10^8 \text{ K}$ in the case of large galaxy clusters (e.g., Vikhlinin et al. 2005; Wallbank et al. 2022); $T_{\infty} \gtrsim 10^7 \text{ K}$ for giant elliptical galaxies like M87 (Di Matteo et al. 2003; Russell et al. 2015); $T_{\infty} \sim 10^6 - 10^7 \text{ K}$ for the Milky Way (Baganoff et al. 2003); and $T_{\infty} \sim 10^6 \text{ K}$ for smaller galaxies (e.g., Ott

et al. 2005).¹ Therefore, from Equation 1, a realistic range of Bondi radii to consider for investigations is $R_B \sim (\text{few} \times 10^4 - \text{few} \times 10^6) r_g$.

2. NUMERICAL METHOD

Our simulations utilize the GRMHD code KHARMA² (“Kokkos-based High-Accuracy Relativistic Magnetohydrodynamics with Adaptive mesh refinement,” Prather 2024). Given a fixed Kerr metric $g_{\mu\nu}$, KHARMA solves the ideal GRMHD equations for the conserved quantities ρu^t , T_μ^t , and B^i . Here, $T^{\mu\nu} = (\rho + u + p_g + b^2) u^\mu u^\nu + (p_g + b^2/2) g^{\mu\nu} - b^\mu b^\nu$ is the energy-momentum tensor of the magnetized gas, ρ is the rest mass density, u is the internal energy density, $p_g = (\gamma_{\text{ad}} - 1)u$ is the gas pressure, b^μ is the magnetic field four-vector, and u^μ is the fluid four-velocity. We refer the reader to Anile (1990); Komissarov (1999); Gammie et al. (2003) for details of the GRMHD equations. As with most GRMHD simulations, radiative effects are ignored, which is a valid approximation for ADAFs with low accretion rates, $\dot{M} \lesssim 10^{-3} \dot{M}_{\text{Edd}}$, where \dot{M}_{Edd} is the Eddington rate.

The multizone method significantly accelerates simulations of problems involving a vast range of length- and time-scales. This is achieved by sequentially iterating between small and large timesteps, allowing each scale to evolve on its own characteristic timescale. Conventional simulations, in contrast, are constrained to use timesteps set by the horizon, which is extraordinarily short compared to the timescale on which any meaningful large-scale evolution occurs. Also, the multizone method is designed to allow sufficient communication between small and large scales, helping the system to efficiently reach a global dynamical equilibrium on all scales. The method is described and tested in detail in Cho et al. (2024, 2025), so here we provide only a brief overview, along with additional numerical details, in Appendix A.

All simulations, except those described in Appendix B, use the same initial conditions (ICs), similar to a spherically symmetric Bondi flow (called **B** IC in Cho et al. 2025). The density is initialized with a profile $\rho_{\text{init}}(r) \propto (r + R_B)/r$ and the temperature T and four-velocity u^μ are set to the general relativistic analytical solution of the hydrodynamic Bondi accretion problem (Michel 1972; Shapiro & Teukolsky 1983). Magnetic fields are initially axisymmetric and nearly vertical, with plasma- $\beta \equiv 2\rho T/b^2$, or gas-to-magnetic pressure ratio,

¹ Su et al. (2025b) find that T_∞ , which is the average temperature in the vicinity of BHs at the limited resolution of cosmological simulations, rarely exceeds 10^8 K.

² <https://github.com/AFD-Illinois/kharma>

of order unity at all radii. There is no gas angular momentum to begin with. However, we note that using ICs with rotating gas or sub-dominant magnetic fields ($\beta \sim 100$) has a minor effect on the final state, as shown in Cho et al. (2025) and demonstrated again in Appendix B. The total duration of each simulation is $700 t_B$ for all runs, unless otherwise stated.

2.1. Diagnostics

For the following analyses, the accretion rate is defined as

$$\dot{M}(r) \equiv - \iint \rho u^r \sqrt{-g} d\theta d\varphi. \quad (2)$$

We choose $\dot{M}(5 r_g)$ as the nominal accretion rate of the BH. The energy inflow rate is $\dot{E}(r) \equiv \iint T_t^r \sqrt{-g} d\theta d\varphi$. The net feedback power is the difference between the energy outflow rate $-\dot{E}$ and the outflow rate of rest-mass energy $-\dot{M}$:

$$\dot{E}_{\text{fb}}(r) \equiv \dot{M} - \dot{E}. \quad (3)$$

The dimensionless feedback efficiency is then

$$\eta(r) \equiv \dot{E}_{\text{fb}}(r) / (\dot{M}(5 r_g) c^2). \quad (4)$$

The kinetic and thermal energy components of the total feedback efficiency are calculated as $\eta_{\text{kinetic}}(r) \equiv (-\iint \rho u^r (u_t + 1) \sqrt{-g} d\theta d\varphi) / (\dot{M}(5 r_g) c^2)$ and $\eta_{\text{thermal}}(r) \equiv (-\iint (u + p_g) u^r u_t \sqrt{-g} d\theta d\varphi) / (\dot{M}(5 r_g) c^2)$, respectively. To estimate the BH spin evolution, we need the angular momentum inflow flux, which is defined as

$$\dot{J}(r) = - \iint T_\varphi^r \sqrt{-g} d\theta d\varphi. \quad (5)$$

Time averages of quantities are indicated with an overbar, e.g., $\bar{\dot{M}}$, $\bar{\dot{E}}_{\text{fb}}$, $\bar{\eta}$. If the radius is not specified, the accretion rate \dot{M} is measured near the horizon at $5 r_g$ and the feedback power \dot{E}_{fb} and efficiency η are measured near the Bondi radius at $R_B/3$.³ The BH mass accretion rate \dot{M} is usually expressed in units of the classic Bondi accretion rate, which for $\gamma_{\text{ad}} = 5/3$ is

$$\dot{M}_B = \pi G^2 M^2 \overline{\rho(R_B)} / c_{s,\infty}^3. \quad (6)$$

When estimating \dot{M}_B , we use the time-averaged gas density, $\overline{\rho(R_B)}$, measured at R_B in the simulation (as in Cho et al. 2024).

³ Following Cho et al. (2025) and out of an abundance of caution, the BH feedback is measured just inside the Bondi radius (at $R_B/3$) because the gas dynamics undergoes a large transition across R_B . In practice, the feedback efficiency $\eta(r)$ remains quite constant as a function of radius, as demonstrated in Figure 2, so the main results are not impacted by where the measurements are made.

3. SUBGRID PRESCRIPTIONS FOR BH ACCRETION AND FEEDBACK

We have carried out BH accretion and feedback simulations with the multizone method for a range of Bondi radii R_B/r_g and BH spin values a_* . The set-up of each simulation is described in Table 1. There is a library of 30 simulations, which consists of 6 BH spin values⁴, $a_* = 0, 0.1, 0.3, 0.5, 0.7, 0.9$, each with 5 choices of the Bondi radius, $R_B/r_g = 400, 2000, 2 \times 10^4, 2 \times 10^5, 2 \times 10^6$. For $R_B/r_g = 2000$, we have additionally simulated an extremely high BH spin value of $a_* = 0.97$. Snapshots of $a_* = 0.9$ runs during the active jet episodes are shown in Figure 6, where the relativistic jets remain collimated as they propagate well beyond several Bondi radii. From the simulations, we estimate the BH mass accretion rate \dot{M}/\dot{M}_B and the feedback power $\dot{E}_{\text{fb}}/\dot{M}_B c^2$, and derive subgrid prescriptions for each.

We present two versions of the BH accretion-feedback subgrid prescription from these GRMHD simulations. The first is a simple time-averaged version (Section 3.1), where we provide analytic formulae for $\dot{M}(R_B, a_*)$ and $\dot{E}_{\text{fb}}(R_B, a_*)$ as functions of the Bondi radius R_B and the BH spin parameter a_* . The second prescription (Section 3.2) takes into account the fact that both accretion and feedback are highly time-variable; therefore, it provides information on the probability distributions of the accretion rate \dot{M} and feedback efficiency η . Depending on the application, we anticipate that one or the other of these prescriptions will be more useful.

Note that our subgrid prescriptions depend on only two parameters: the dimensionless Bondi radius R_B/r_g (or equivalently, the gas temperature T_∞ beyond the Bondi radius, see Equation 1), and the BH spin parameter a_* . There is no dependence on any other gas properties outside the Bondi radius. As demonstrated in Cho et al. (2024, 2025) and in Appendix B here, the dynamical equilibrium state reached over a long runtime is independent of the initial gas configuration, gas rotation, or magnetic field strength. Thus, our BH subgrid models make no distinction between prograde and retrograde ICs, nor between strongly magnetized (MAD) and weakly magnetized (SANE) conditions.

3.1. Prescription 1: Time-averaged accretion-feedback

The time-averaged accretion rate \dot{M} , feedback power \dot{E}_{fb} , and feedback efficiency $\bar{\eta}$ for all runs are shown in

⁴ For the non-spinning case ($a_* = 0$), the run with the largest Bondi radius ($R_B = 2 \times 10^6 r_g$) was evolved for a shorter duration of $500 t_B$. Nevertheless, it reaches a final state consistent with our previous work (Cho et al. 2024).

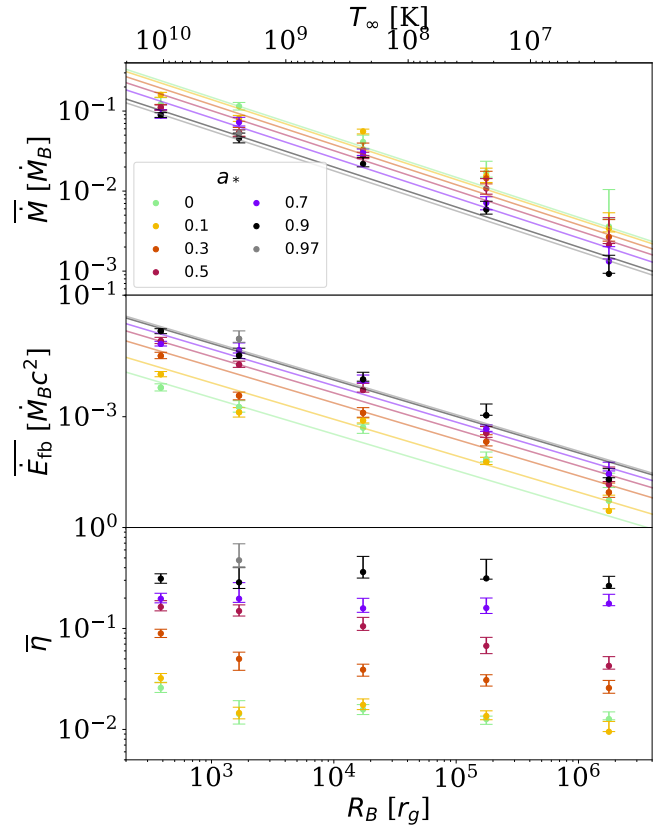


Figure 1. Time averaged accretion rate \dot{M} (top), feedback power \dot{E}_{fb} (middle), and feedback efficiency $\bar{\eta}$ (bottom), for simulations with varying Bondi radii R_B and BH spins a_* . The scale at the bottom shows the Bondi radius R_B in units of the gravitational radius r_g , and the scale at the top shows the corresponding asymptotic temperature T_∞ . Colors represent different BH spins. The approximate formulae for \dot{M} (Equation 7) and \dot{E}_{fb} (Equation 8) are shown as straight lines in the top and middle panels.

Figure 1, and their numerical values are listed in Table 2. The calculation of error bars is explained in Appendix D. In concordance with previous work, we find that the BH accretion rate scales with the Bondi radius roughly as $\dot{M}/\dot{M}_B \propto (R_B/r_g)^{-0.5}$. For a given Bondi radius R_B , there is a mild dependence of \dot{M} on the BH spin, e.g., \dot{M} is a factor of a few lower for $a_* = 0.9$ compared to $a_* = 0$, again consistent with previous works (e.g., Guo et al. 2025; Cho & Narayan 2025; Cho et al. 2025). For $a_* = 0.9$, we reproduce one of the main results of Cho et al. (2025), namely, that the time-averaged feedback efficiency, $\bar{\eta} \approx 0.3$, is insensitive to the Bondi radius R_B .

In the top panel of Figure 1, there is evidence for some curvature in the variation of $\log(\dot{M}/\dot{M}_B)$ vs $\log(R_B/r_g)$. However, for simplicity, we fit the measured values to

$R_B [r_g]$	n	$r_{\text{out}} [r_g]$	Time-averaged (§ 3.1)	Distribution (§ 3.2)	Spin evolution (§ 4)
≈ 400	4	$8^7 \approx 2 \times 10^6$	$\overline{\dot{M}}(R_B, a_*)$ (7)		
≈ 2000	5	$8^9 \approx 10^8$		$\ln \dot{M} \sim \mathcal{N}(\mu_{\ln \dot{M}}, \sigma_{\ln \dot{M}}^2)$	
$\approx 2 \times 10^4$	6	$8^9 \approx 10^8$			spinup $\overline{s}(a_*)$ (10)
$\approx 2 \times 10^5$	7	$8^{10} \approx 10^9$	$\overline{\dot{E}_{\text{fb}}}(R_B, a_*)$ (8)	$\ln \eta \sim \mathcal{N}(\mu_{\ln \eta}, \sigma_{\ln \eta}^2)$	
$\approx 2 \times 10^6$	8	$8^{11} \approx 10^{10}$			

Table 1. Set-up of the multizone GRMHD simulations, and summary of the main results. The first three columns list the Bondi radius R_B , the number of zones n , and the outermost radius of the simulation r_{out} . For each R_B , we perform simulations for 6 BH spin values, $a_* = 0, 0.1, 0.3, 0.5, 0.7, 0.9$. The last three columns reference the sections and equations presenting the main results of this paper: two BH subgrid prescriptions (time-averaged quantities and their distributions) and the rate of evolution of BH spin.

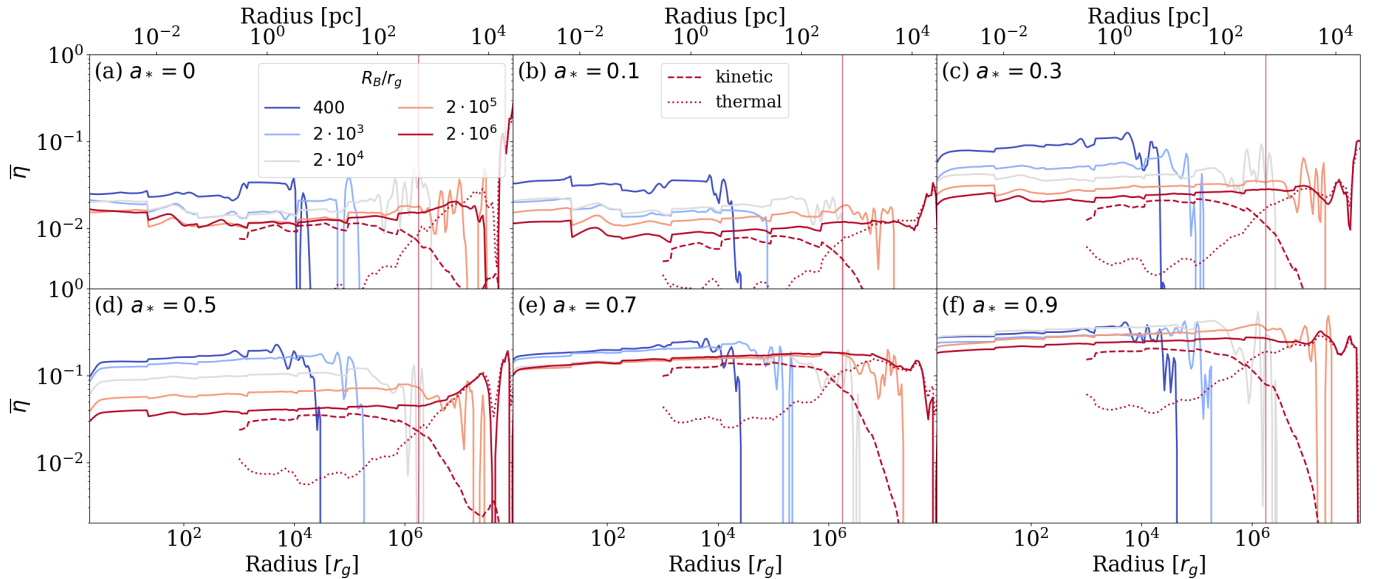


Figure 2. Radial profiles of the time-averaged feedback efficiency $\overline{\eta}(r)$. Each panel corresponds to a single BH spin a_* and colors represent different Bondi radii R_B . The scale at the bottom shows the radius in units of r_g , and the scale at the top shows the physical radius in pc for M87's BH mass. For the largest Bondi radius, $R_B = 2 \times 10^6 r_g$, the kinetic $\overline{\eta}_{\text{kinetic}}(r)$ (dashed) and thermal $\overline{\eta}_{\text{thermal}}(r)$ (dotted) components are also overplotted, showing the conversion of kinetic to thermal energy as the jet outflow crosses R_B (vertical lines).

straight lines. Furthermore, even though the best-fit lines have slightly different slopes, we assume the same slope for all spins, to obtain the following subgrid prescription⁵ for the time-averaged mass accretion rate of the BH:

$$\overline{\dot{M}} \approx (-3|a_*| + 4.7) \left(\frac{R_B}{r_g} \right)^{-0.5}. \quad (7)$$

Similarly, from the measurements shown in the middle panel of Figure 1, we find that the time-averaged

feedback power $\overline{\dot{E}_{\text{fb}}}$ exhibits a similar power law scaling $\propto R_B^{-0.6}$ for all BH spins a_* . This gives the following approximate subgrid prescription for the feedback power,

$$\frac{\overline{\dot{E}_{\text{fb}}}}{M_B c^2} \approx (0.98|a_*| + 0.13) \left(\frac{R_B}{r_g} \right)^{-0.6}. \quad (8)$$

These approximate subgrid prescriptions for $\overline{\dot{M}}$ and $\overline{\dot{E}_{\text{fb}}}$ are shown as straight lines in the top and middle panels of Figure 1. Interestingly, our fit suggests that the feedback power depends linearly on the BH spin a_* , not quadratically as we would expect from force-free models of the jet (Blandford & Znajek 1977; Tchekhovskoy et al. 2010, 2011). While the reason is unclear, we note that the feedback power we are considering is the average of

⁵ After fitting $\overline{\dot{M}}$ and $\overline{\dot{E}_{\text{fb}}}$ assuming the same R_B scaling for each BH spin, we fit their coefficients as a linear function of a_* to obtain Equations 7 and 8.

a highly time-variable quantity, whereas the analytical theory describes a perfectly time-steady phenomenon.

In the bottom panel of Figure 1, the feedback efficiencies $\bar{\eta}$ are shown for all the runs. While rapidly spinning BHs have feedback efficiencies $\bar{\eta}$ independent of the Bondi radius, e.g., $\bar{\eta} \approx 0.3$ for $a_* = 0.9$ and $\bar{\eta} \approx 0.2$ for $a_* = 0.7$; slowly spinning BHs ($a_* \lesssim 0.5$) show a mild dependence on the Bondi radius, $\bar{\eta} \propto (R_B/r_g)^{-0.2}$.⁶ It is possible that the weaker jets associated with slower spinning BHs have more difficulty competing with the large-scale inflowing matter and therefore perhaps there is a decline in feedback efficiency for larger R_B . Moreover, the slowest spinning case, $a_* = 0.1$, exhibits nearly the same feedback efficiency as the $a_* = 0$ model, indicating that the jet is subdominant to the baseline level of feedback in the nonspinning case, which is associated with reconnection-driven convection (Cho et al. 2023).

Radial profiles of the time-averaged feedback efficiency $\bar{\eta}(r)$ are shown in Figure 2, where each panel corresponds to a single BH spin a_* .⁷ For all runs, the feedback efficiency $\bar{\eta}(r)$ remains constant out to a few Bondi radii, indicating that each multizone simulation has achieved a global dynamical equilibrium. The previously noted difference in behavior between low and high BH spins is seen again in the $\bar{\eta}(r)$ profiles. The runs with slowly spinning BHs, $a_* = 0.1, 0.3, 0.5$, have a wider spread in their $\bar{\eta}$ values with changing Bondi radius R_B , whereas for the runs with high BH spins, $a_* = 0.7, 0.9$, the profiles are in close agreement between different R_B for a given a_* .

At the Bondi radius R_B , kinetic and thermal components of the feedback efficiency $\bar{\eta}$ are nearly in equipartition, with $\bar{\eta}_{\text{kinetic}} \approx \bar{\eta}_{\text{thermal}} \approx \bar{\eta}/2$ for all runs. Inside R_B , the kinetic component dominates, while outside R_B , the thermal energy becomes dominant, as shown in Figure 2. This is not surprising, since the Bondi radius R_B marks a transition point where the outflowing jet, which up to this point has propagated through a confining medium with a steeply declining pressure, suddenly encounters an extended layer of constant gas density and pressure. It is reasonable for the kinetic energy of the feedback to be converted to thermal energy at this point. However, it remains to be tested whether

⁶ For the non-spinning case $a_* = 0$, $\bar{\eta}$ seems to again have a very weak dependence on the Bondi radius R_B , with $\bar{\eta} \sim 0.01$, consistent with our earlier work (Cho et al. 2024).

⁷ The jumps in feedback efficiency $\eta(r)$ across zones are reduced here compared to our previous work (e.g., see Fig. 8 in Cho et al. 2025). This is due to our use of the improved inversion scheme of Kastaun et al. (2021) described in Appendix A.3, which avoids inversion failures.

this behavior persists in realistic galactic environments beyond the Bondi radius.

3.2. Prescription 2: Distribution of accretion-feedback

Here we present a more complete description of the statistical properties of \dot{M} and η . For spinning BHs ($a_* \neq 0$) with large Bondi radii R_B , the accretion rate \dot{M} and feedback efficiency η can fluctuate strongly by over 2 orders of magnitude (Cho et al. 2025, see also Guo et al. 2025). Therefore, the probability distributions of \dot{M} and η better represent the time-varying BH accretion and feedback, compared to the simple time-averages considered in Section 3.1.

The distributions of the logarithm of the accretion rate, \dot{M}/\dot{M}_B , and the feedback efficiency, η , are shown for a subsample of runs in Figure 3. Both quantities have approximately lognormal distributions, with standard deviation σ increasing with increasing Bondi radius R_B . The complete list of means and standard deviations of $\ln(\dot{M}/\dot{M}_B)$ and $\ln(\eta)$ is provided in Table 2.

Interestingly, for high BH spins, $a_* = 0.7, 0.9$, the peak of the $\ln(\eta)$ distribution shifts substantially between $R_B \approx 400 r_g$ and $R_B \approx 2 \times 10^6 r_g$ (see the two right panels in the bottom row). At first glance, this appears to contradict Section 3.1, where the time averaged efficiency $\bar{\eta}$ for these spin values was shown to be independent of the Bondi radius R_B . This apparent inconsistency can be understood through the properties of the lognormal distribution, as explained in Appendix D. If a statistical variable X follows a lognormal distribution, the mean of X is determined by a combination of the mean and standard deviation of $\ln X$ (Equation D10). Therefore, the decreased mean $\mu_{\ln \eta}$ for large R_B is compensated by an increased spread $\sigma_{\ln \eta}$, leading to similar average efficiencies $\bar{\eta}$. The estimated means calculated using Equation D10 are shown as vertical bars in Figure 3. The values for $R_B = 400 r_g$ and $2 \times 10^6 r_g$ indeed agree well for $a_* = 0.7$ and 0.9 , despite the two underlying distributions being very different. This is consistent with Section 3.1.

4. BH SPIN EVOLUTION

A feature of the subgrid prescriptions developed in this paper is that they depend on the BH spin parameter a_* . In order for cosmological simulations and SAMs to use these prescriptions, they will need to follow the spin evolution of SMBHs over cosmological timescales. For this, they need prescriptions for the rate of change of BH spin, da_*/dt , corresponding to each accretion scenario.

Our GRMHD simulations assume a fixed a_* for each run, which is reasonable since the spindown timescale for the low Eddington ratio accretion we consider is much

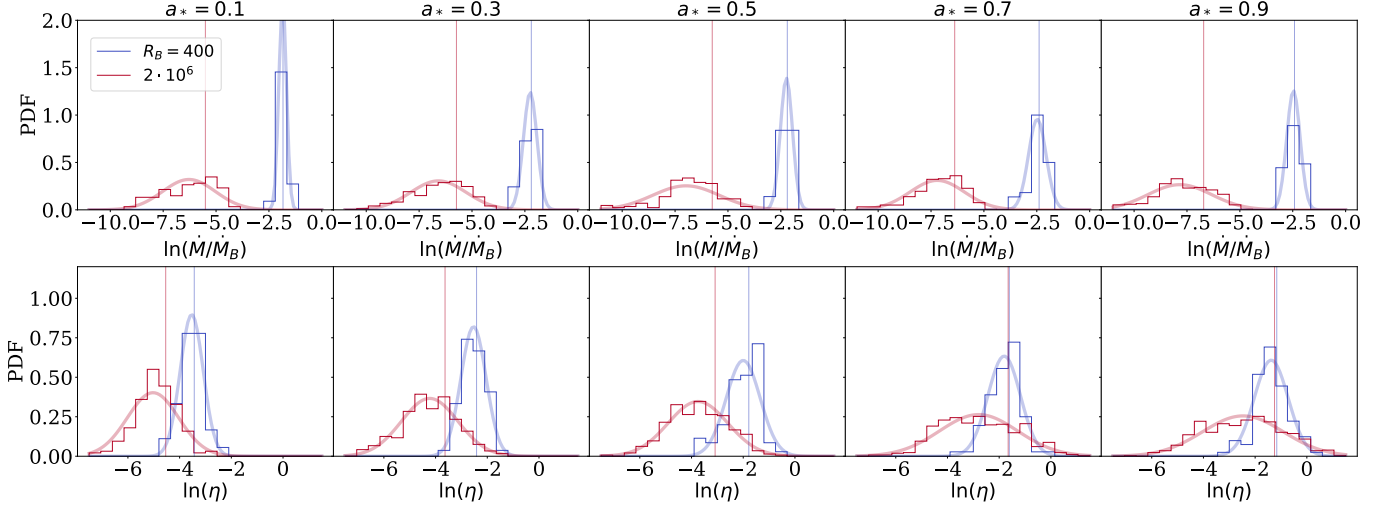


Figure 3. Distributions of $\ln(\dot{M}/\dot{M}_B)$ (top row) and $\ln(\eta)$ (bottom row). Each column is for a given BH spin a_* and the blue and red curves are for the smallest and largest Bondi radii, $R_B \approx 400 r_g$ and $\approx 2 \times 10^6 r_g$, respectively. Lognormal curves corresponding to each run are overplotted for comparison. The means of the lognormal variable X , calculated using Equation D10 from log-space quantities $\mu_{\ln X}$ and $\sigma_{\ln X}$, are shown as vertical lines.

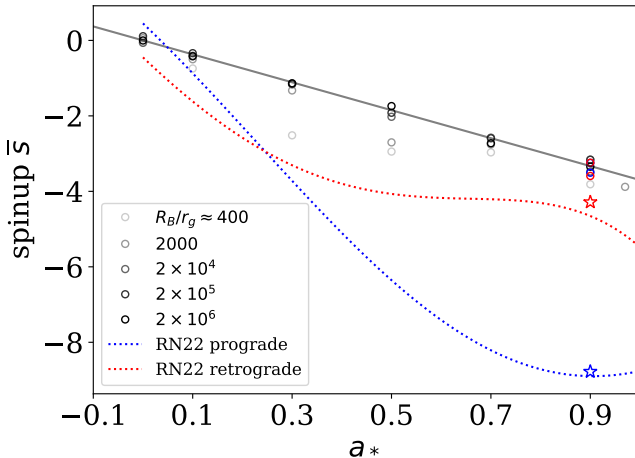


Figure 4. The spinup parameter s (Equation 9) as a function of BH spin a_* . Fiducial runs without initial gas angular momentum are shown in grayscale. Blue and red open circles represent runs with initially co- and counter-rotating gas, respectively, and agree well with the equivalent fiducial runs without rotation. RN22’s small-scale GRMHD simulations are shown as dotted lines for prograde (blue) and retrograde (red). Multizone simulations limited to much shorter durations from Cho et al. (2025), shown as stars, agree better with the RN22 curves.

longer (> 1 Gyr, e.g., Narayan et al. 2022, hereafter RN22) than our simulation runtime $700 t_B \approx 50$ Myr (assuming an M87-like system with a Bondi radius $R_B \approx 2 \times 10^5 r_g$). However, our simulations do pro-

vide information on da_*/dt via the angular momentum inflow flux \dot{J} defined in Equation 5.

The dimensionless spinup parameter s is defined as (Gammie et al. 2004; Shapiro 2005)

$$s \equiv \frac{da_*}{dt} \frac{M}{\dot{M}}, \quad (9)$$

where $j \equiv (\dot{J}/\dot{M})(5 r_g)$ is the specific angular momentum inflow rate and $e \equiv (\dot{E}/\dot{M})(5 r_g)$ is the specific energy inflow rate into the BH. In Figure 4, the time-averaged spinup parameters \bar{s} corresponding to all runs are shown as gray dots, with light to bold shades signifying increasing Bondi radius R_B . All spinup parameters are negative, meaning that, in every case, the BH undergoes spindown.⁸ Interestingly, runs with realistic Bondi radii $R_B = 2 \times 10^4 - 2 \times 10^6 r_g$ give very similar spinup parameter values, so we can assume that \bar{s} depends only on the BH spin a_* . Fitting a line through runs with $R_B = 2 \times 10^4 - 2 \times 10^6 r_g$, we obtain the following simple formula for the spinup parameter,

$$\bar{s}(a_*) \approx -3.7 a_*, \quad (10)$$

shown as the black line in Figure 4.

Additionally, we also show the runs with prograde and retrograde ICs discussed in Appendix B, with blue and red circles, respectively. The spinup parameters s are

⁸ Since there is no initial gas rotation, by symmetry, the same conclusion holds for negative spins: the BH spin slows down ($|a_*|$ decreases) in which case the spinup parameter is positive $s > 0$.

similar for all ICs, regardless of the initial gas angular momentum. This again demonstrates the robustness of the final dynamical equilibrium, independent of the initial gas configuration (Cho et al. 2024, 2025, and Appendix B).

For completeness, we compare our results with conventional small-scale GRMHD simulations. RN22 conducted a survey of a number of BH spins a_* , initialized with a small-scale torus of characteristic size $\sim 40 r_g$ (radius of the pressure maximum). Their fitted spinup parameters (Equation 15 in RN22) are plotted in Figure 4 as blue (prograde) and red (retrograde) dotted lines. Our multizone simulations do not agree with either of these curves.

The difference between our multizone runs and previous GRMHD simulations can be understood along the lines of the discussion in Cho & Narayan (2025). The runtime of most GRMHD simulations with torus ICs, including RN22, is less than or at best marginally equal to the time it takes the corresponding systems to reach their final state of strong variability.⁹ On the other hand, when simulations are run for a much longer duration using the multizone method, the strongly variable state is always reached: the flow then alternates between prograde and retrograde states and the jet becomes intermittent. This explains the smaller values of $|\bar{s}|$ we find in our multizone simulations. Switching signs of the gas angular momentum leaves a negligible effect on the BH spin evolution. In addition, intermittency in the jet power makes extracting BH's spin energy less efficient. Together, these effects decrease the magnitude of the BH spindown parameter $|\bar{s}|$.

As a test, we compare our results with small-scale ($R_B \approx 400 r_g$) multizone simulations from Cho et al. (2025) where the runtimes were reduced to $50 t_B$ and magnetic fields were initially weak to reproduce typical GRMHD simulations (runs labeled as `mz+` and `mz-` in their work). The spinup parameters obtained from these runs are shown in Figure 4 as blue and red stars for co-rotating and counter-rotating ICs, respectively. Indeed, when the runtime is much shortened, we recover spinup parameters similar to those of RN22's for prograde and retrograde. These results demonstrate that direct use of GRMHD simulations as subgrid prescriptions should be treated with caution, since typical GRMHD results

probe much shorter timescales and may not capture the dynamical equilibrium reached over galactic timescales.

The BH spindown timescale can be calculated as

$$t_s \equiv \left| \frac{a_*}{da_*/dt} \right| = \frac{a_*}{f_{\text{Edd}} \frac{\dot{M}_{\text{Edd}}}{M} |\bar{s}(a_*)|}, \quad (11)$$

where the second equality uses the definition of s in Equation 9. Here, $f_{\text{Edd}} = \dot{M}/\dot{M}_{\text{Edd}}$ is the Eddington ratio, and $M/\dot{M}_{\text{Edd}} \equiv t_S$ is a BH mass independent constant, the Salpeter time $t_S = 4.5 \times 10^7$ yr. Substituting Equation 10 for $\bar{s}(a_*)$, we find that the spindown timescale depends only on the accretion rate as

$$t_s = 12 \left(\frac{10^{-3}}{f_{\text{Edd}}} \right) \text{ Gyr}, \quad (12)$$

which is longer than the time scale of a few Gyr derived in previous GRMHD work (Narayan et al. 2022; Ricarte et al. 2023). For $f_{\text{Edd}} \approx 10^{-3}$, the spindown timescale is already comparable with the Hubble time, and it is even longer for systems like M87 with $f_{\text{Edd}} \lesssim 10^{-4}$. This implies that BH spin evolution occurs mostly during periods of rapid accretion ($f_{\text{Edd}} \sim 0.1 - 1$), or via BH mergers. When the BH enters the low-Eddington ratio phase $f_{\text{Edd}} \lesssim 10^{-3}$, however, the BH spin is nearly fixed at a constant value until its next highly accreting phase.

5. CONCLUSIONS & DISCUSSION

Building on the multizone GRMHD framework developed in our earlier work, we have constructed a library of long-duration simulations that *self-consistently* couples horizon-scale accretion physics to galactic scales across an unprecedented dynamic range. The suite spans BH spins $|a_*| = 0-0.9$ and Bondi radii $R_B \simeq 4 \times 10^2 - 2 \times 10^6 r_g$, enabling the systematic derivation of first-principles, spin-dependent subgrid prescriptions appropriate to hot, radiatively inefficient accretion flows at low Eddington ratios ($f_{\text{Edd}} \lesssim 10^{-3}$).

From this parameter study, we provide two complementary subgrid models for cosmological simulations and SAMs:

- Time-averaged prescriptions: We supply compact analytic fits for the suppressed mean accretion rate and the mean feedback power, normalized to the classic Bondi rate \dot{M}_B (cf. Equation 6). In our simulations, both \bar{M}/\dot{M}_B and $\bar{E}_{\text{fb}}/(\dot{M}_B c^2)$ follow simple power-law scalings with R_B , with coefficients that vary linearly with spin (Equations 7

⁹ Cho & Narayan (2025) found that the onset time of strong variability increases with increasing initial rotation-to-magnetic energy ratio, $\mathcal{R} \equiv \rho r^2 \Omega^2 / b^2$. According to their prediction, the total runtime $10^5 t_g$ of RN22 is insufficient to reach the final state of strong variability.

and 8):

$$\frac{\dot{\bar{M}}}{\dot{M}_B} \approx (-3|a_*| + 4.7) \left(\frac{R_B}{r_g} \right)^{-0.5},$$

$$\frac{\dot{\bar{E}}_{\text{fb}}}{\dot{M}_B c^2} \approx (0.98|a_*| + 0.13) \left(\frac{R_B}{r_g} \right)^{-0.6}.$$

A key qualitative outcome is that higher-spin BHs deliver larger feedback power at fixed R_B , while exhibiting modestly lower accretion rates, consistent with a stronger jet/outflow regulating inflow on large scales.

- Stochastic (distribution-level) prescriptions: As accretion and feedback are intrinsically and strongly time-variable—especially for larger R_B and nonzero spin—we additionally characterize the *full* probability distributions of \dot{M} and η . Both are well described by lognormal statistics, with the width (scatter in $\ln \dot{M}$ and $\ln \eta$) increasing with R_B . We tabulate the corresponding means and variances for all models in Table 2, enabling applications that require bursty coupling rather than relying solely on time-averaged properties.

Since our accretion-feedback prescription is explicitly spin-dependent, we also quantify BH spin evolution in the low- f_{Edd} regime. Using the angular-momentum fluxes measured in the simulations, we find that the spinup parameter is well approximated by a simple linear function of a_* (Equation 10),

$$s(a_*) \simeq -3.7 a_*,$$

implying spindown in this hot-mode state. The associated spindown timescale is extremely long (Equation 12),

$$t_s \simeq 12 \left(\frac{10^{-3}}{f_{\text{Edd}}} \right) \text{Gyr},$$

so for $f_{\text{Edd}} \lesssim 10^{-3}$ the spin is effectively “frozen” over cosmological times. Thus, spin changes are expected to occur primarily during high-accretion episodes and/or mergers, not during quiescent ADAF phases.

The subgrid prescription developed in Section 3.1 is designed for direct use in cosmological simulations and SAMs, provided the BH is in the low-Eddington, hot-accretion regime ($f_{\text{Edd}} \lesssim 10^{-3}$). At higher accretion rates, where the flow is expected to transition to a radiatively efficient state, a different accretion/feedback model should be adopted. We envision the implementation of these schemes into simulations & SAMs proceeding as follows:

1. Estimate the Bondi scale: Determine the Bondi radius in gravitational units, R_B/r_g , by measuring the average gas temperature T_∞ in the BH’s vicinity as resolved in cosmological models (which typically exceed the Bondi radius scales) via Equation 1. In practice, this step highlights a common limitation of large-volume runs: the Bondi radius is often only marginally resolved, and the inferred T_∞ (hence R_B) can be sensitive to the adopted measurement aperture and subgrid ISM treatment.
2. Compute the Bondi inflow rate: Measure the gas density ρ at the Bondi scale (or estimate it from the local density if unresolved) and compute the Bondi accretion rate \dot{M}_B using Equation 6.
3. Apply the suppression of accretion: Use the calibrated scaling in Equation 7 to obtain the suppressed accretion rate \dot{M} relative to \dot{M}_B , and evolve the BH mass by \dot{M} .
4. Inject feedback power: Compute the feedback power \dot{E}_{fb} from Equation 8 and couple it to the surrounding gas. If possible, a collimated (bipolar) injection geometry is the most physically motivated choice for hot-mode feedback (see Figure 6).
5. Evolve the BH spin: Update the BH spin a_* using the fitted spin-evolution relation in Equation 10.

Finally, our results, together with Cho et al. (2025), underscore a central cautionary lesson: short-duration, small-domain GRMHD simulations can mis-estimate long-term, galaxy-scale behavior when directly repurposed as subgrid models. The multizone approach reaches a global dynamical equilibrium over scales extending beyond R_B , and captures the strong variability of the equilibrated state (including jet intermittency and an effective loss of initial rotational memory) that materially alters the inferred mean energetics and spin evolution compared to conventional small-scale GRMHD simulations. This is precisely what makes the present prescriptions robust and directly portable: the feedback power measured near the Bondi radius R_B is obtained in a self-consistent, equilibrated inflow–outflow system and, therefore, can be transferred to larger-scale cosmological calculations without uncontrolled extrapolation.

We note some caveats of this work. Here, we considered BH spins in the range $|a_*| = 0–0.9$, so the formulae for $\dot{M}(R_B, a_*)$, $\dot{E}_{\text{fb}}(R_B, a_*)$, and $s(a_*)$ (Equations 7, 8, 10) are not validated for near-maximal BH spins. In addition, because our GRMHD framework neglects radiative effects, the resulting BH subgrid prescriptions

are applicable only to low- \dot{M} ADAF states, as radiative cooling may already influence accretion flows starting at $\dot{M} \gtrsim 10^{-5} \dot{M}_{\text{Edd}}$ (Singh et al. 2025). For discussions of the accretion rate \dot{M} threshold below which ADAF states are expected, see, e.g., Yuan & Narayan (2014); Cho & Narayan (2022). Finally, we adopt primarily vertical magnetic field geometries. Although large-scale poloidal fields are expected to arise naturally in realistic environments (e.g., Liska et al. 2020), alternative magnetic configurations (e.g., toroidal or randomized) deserve further study. The caveats of the multizone method itself are described extensively in Cho et al. (2024, 2025) and are not repeated here.

By bridging horizon-scale physics to galactic scales via the multizone method, this work establishes a physically grounded foundation for spin-dependent BH subgrid models in next-generation cosmological simulations and SAMs. These prescriptions for low accretion modes will be particularly useful for models that explicitly track BH spin evolution (e.g., NEWHORIZON Dubois et al. 2021; Beckmann et al. 2025, AREPO Talbot et al. 2021, COLIBRE Schaye et al. 2025; Huško et al. 2025).

ACKNOWLEDGEMENTS

H.C., B.P., R.N., K.S., A.R., and P.N. were partially supported by the Black Hole Initiative at Harvard University, which is funded in part by the Gordon and Betty Moore Foundation (Grant #13526). It was also made possible through the support of a grant from the John Templeton Foundation (Grant #63445). The opinions expressed in this publication are those of the author(s) and do not necessarily reflect the views of these Foundations. This publication is funded in part by the Gordon and Betty Moore Foundation, Grant GBMF-12987. A.P.V. gratefully acknowledges support from the National Science Foundation Astronomy & Astrophysics Postdoctoral Fellowship under Award Number 2502826. This work used Delta at the University of Illinois at Urbana Champaign through allocation PHY250303 from the Advanced Cyberinfrastructure Coordination Ecosystem: Services & Support (ACCESS) program, which is supported by U.S. National Science Foundation grants #2138259, #2138286, #2138307, #2137603, and #2138296.

APPENDIX

A. OVERVIEW OF THE MULTIZONE METHOD AND ADDITIONAL NUMERICAL DETAILS

A.1. *Multizone Method*

In the multizone method, the full simulation domain, extending from $r = r_g$ to r_{out} , is divided into different subregions, or zones, and evolved in a manner similar to a “V-cycle”. Each zone- i has a different inner radius, $r_{i,\text{in}} = 8^i r_g$, and a common outer radius, $r_{i,\text{out}} = r_{\text{out}}$, where r_{out} is chosen to be much larger than the Bondi radius R_B (see Table 1). For n zones, the method begins by evolving the outermost zone- $(n-1)$. Then, the active zone is switched sequentially to zone- $(n-2)$, zone- $(n-3)$, …, down to zone-0, which incrementally moves the inner boundary inwards down to $r = r_g$. This constitutes the inward moving half of the V-cycle, which tracks accretion. The inner boundary is then moved back out from zone-0 to zone- $(n-1)$, completing one full V-cycle. The second half of the V-cycle captures the outflowing part of the communication or feedback. For a given simulation, V-cycles are repeated over a few tens to hundreds of times to ensure enough communication between small and large scales (see the third column of Table 2 for the total number of V-cycles for each run). Following Cho et al. (2025), each zone is evolved for a duration of $8000\Delta t$ before switching to the next zone, where Δt is the on-the-fly calculated timestep set by the Courant condition for that zone. For zone-0, which covers the whole simulation domain, we run 10 times longer ($80000\Delta t$) to allow for extra relaxation. Tests of different choices of the zone boundaries and runtime per zone are described in Appendix F of Cho et al. (2024).

Besides the usual simulation boundaries at r_g and r_{out} , the multizone scheme introduces additional internal radial boundaries at $r_{i>0,\text{in}}$. These internal boundaries are assigned Dirichlet boundary conditions such that ρ , u , u^μ , and B^i are held constant over the duration of each zone. Importantly, for the magnetic fields, we apply an additional prescription, labeled `bflux-const` in Cho et al. (2024, 2025), to the electric fields on the internal radial boundary face. This prescription ensures the divergence-free condition, $\nabla \cdot \vec{B} = 0$, and avoids destructive magnetic tension between active and inactive regions. For implementation details and tests of the `bflux-const` prescription, see Appendix E of Cho et al. (2024) and Section 3 of Cho et al. (2025). At the innermost radius, $r = r_{0,\text{in}} = r_g$, which lies inside the BH horizon, the gas is allowed to flow freely towards the singularity. Similarly, gas can freely leave the simulation domain at the outermost radius, $r = r_{\text{out}}$. In the θ and φ directions, we use reflecting and periodic boundary conditions, respectively.

The key strength of the multizone method is that it significantly lowers the computational cost of these large dynamic range simulations. This is achieved by periodically freezing and unfreezing the inner scales inside $r_{i,\text{in}}$, thereby permitting a larger timestep suitable for the currently active radial range. The multizone method’s careful design of progressively moving the interior boundary $r_{i,\text{in}}$ in and out allows each scale to respond to any information transferred from both inner and outer scales. Thus, a global dynamical equilibrium is quickly reached with a reasonable computational cost.

A.2. *Other Numerical Set-up*

The numerical set-up in the present work is identical to that in Cho et al. (2025), except for the inversion scheme. In Cho et al. (2025), the 1D_W inversion scheme (Noble et al. 2006; Mignone & McKinney 2007) was used, where occasional inversion failures at the internal boundaries resulted in jumps in the radial profile for the efficiency $\eta(r)$. Here, we adopt the more robust inversion scheme of Kastaun et al. (2021) which avoids such failures. We made some modifications to their original Kastaun et al. (2021) scheme to avoid problematic high velocity cells during the inversion (details are given in Appendix A.3). We adopt face-centered magnetic fields and the same set of floors as in Cho et al. (2025).

We adopt an exponential Kerr-Schild (EKS) coordinate system where the grid is evenly spaced in $\log r$, θ , φ . This naturally focuses the spatial resolution closer to the BH. To avoid unnecessarily short timesteps from small φ edges of cells near the polar axes ($\theta = 0, \pi$), we use an internal static mesh refinement (ISMR) scheme that de-refines cells in the φ direction. The ISMR implementation details are presented in Cho et al. (2025). For the resolution of $N_r \times N_\theta \times N_\varphi = 32 \log_8(r_{\text{out}}/r_g) \times 64 \times 64$, where r_{out} is the outermost radius of the simulation, ISMR is used on 4 layers of the θ grid near each pole.

Time-averaged quantities are calculated over the latter half of the total runtime (i.e., $t = 350 - 700 t_B$). The time-averages are calculated for each zone individually, using the final snapshot of each zone before switching zones, in order to minimize the imprint of internal boundaries. Then, we combine zone- i 's time-averages at radii $8^{0.5} r_{i,\text{in}} - 8^{1.5} r_{i,\text{in}}$, except for zone-0 and zone- $(n-1)$ where the range extends to the innermost radius $r_{0,\text{in}}$ and outermost radius r_{out} of the simulation, respectively.

A.3. Momentum Conserving Inversion Scheme

The technical improvement of this work relative to Cho et al. (2025) is the adoption of the Kastaun et al. (2021) inversion scheme that prevents discontinuities in the outflow power across zones. Here we describe our slightly modified implementation of the scheme. In Kastaun et al. (2021), the primitives $\mathbb{P} = \{\rho, u, v^i, B^i\}$ are inverted from conserved quantities in the Eulerian frame: density $-\rho u^\mu n_\mu = \rho\Gamma$, net energy density $n_\alpha n_\beta T^{\alpha\beta} + \rho u^\alpha n_\alpha$, three-momentum density $-\gamma_i^\mu n^\alpha T_{\alpha\mu} = \alpha T_i^t$, and magnetic fields. For a given set of conserved variables $\{\rho\Gamma, n_\alpha n_\beta T^{\alpha\beta} + \rho u^\alpha n_\alpha, \alpha T_i^t, B^i\}$, the scheme finds a unique solution of \mathbb{P} . While the resulting solution is reasonable in most cases, the inversion occasionally produces extremely low internal energy u and extremely fast velocities v^i , in the strongly magnetized regions $\beta \ll 1$. In such problematic cases where the Kastaun et al. (2021) scheme inverted velocity exceeds the desired maximum Lorentz factor Γ_{max} , we instead apply the following inversion that conserves only the momentum density T_i^t and magnetic fields B^i , sacrificing conservation of density and net energy density – that is, inserting new density and internal energy in the coordinate frame. The new scheme is described below.

First, we separate the momentum density $S_i = \alpha T_i^t$ into parallel and perpendicular components with respect to magnetic fields.

$$S_\parallel^i = \rho h \Gamma^2 v_\parallel^i, \quad S_\perp^i = (\rho h \Gamma^2 + B^2) v_\perp^i, \quad (\text{A1})$$

where $h = 1 + \gamma_{\text{ad}} u / \rho$ is the specific enthalpy, v_\parallel and v_\perp are parallel and perpendicular velocities to magnetic fields respectively. Then, when expressing the magnitude of velocity in terms of the momentum density,

$$v^2 = \frac{S_\parallel^2}{(\rho h \Gamma^2)^2} + \frac{S_\perp^2}{(\rho h \Gamma^2 + B^2)^2}, \quad (\text{A2})$$

the above is equal to $1 - 1/\Gamma^2$. Then we solve for the function

$$f(\Gamma) = \frac{S_\parallel^2}{(\rho h \Gamma^2)^2} + \frac{S_\perp^2}{(\rho h \Gamma^2 + B^2)^2} + \frac{1}{\Gamma^2} - 1 = 0. \quad (\text{A3})$$

The function $f(\Gamma)$ has a nice property that it monotonically decreases $f'(\Gamma) < 0$ and $f(1) > 0$. Therefore, in order for $f(\Gamma)$ to have a solution in the range $\Gamma \in [1, \Gamma_{\text{max}}]$, we need to ensure that $f(\Gamma_{\text{max}}) < 0$. For a given S_\parallel , S_\perp , \vec{B} , the condition $f(\Gamma_{\text{max}}) < 0$ constrains the value of ρh . If we assert that

$$f(\Gamma_{\text{max}}) < \frac{S_\parallel^2}{(\rho h)^2 \Gamma_{\text{max}}^4} + \frac{S_\perp^2}{(\rho h)^2 \Gamma_{\text{max}}^4} + \frac{1}{\Gamma_{\text{max}}^2} - 1 < 0, \quad (\text{A4})$$

ρh should be greater than

$$\rho h > \frac{S}{\Gamma_{\text{max}}^2 \sqrt{1 - 1/\Gamma_{\text{max}}^2}} = (\rho h)_{\text{min}}. \quad (\text{A5})$$

The implementation order of the modified Kastaun et al. (2021) scheme is as follows. After Kastaun et al. (2021) inversion, if ρh is smaller than $(\rho h)_{\text{min}}$, ρ and u are increased proportionally to conserve the temperature

$$\rho \rightarrow \rho \frac{(\rho h)_{\text{min}}}{\rho h}, \quad u \rightarrow u \frac{(\rho h)_{\text{min}}}{\rho h}. \quad (\text{A6})$$

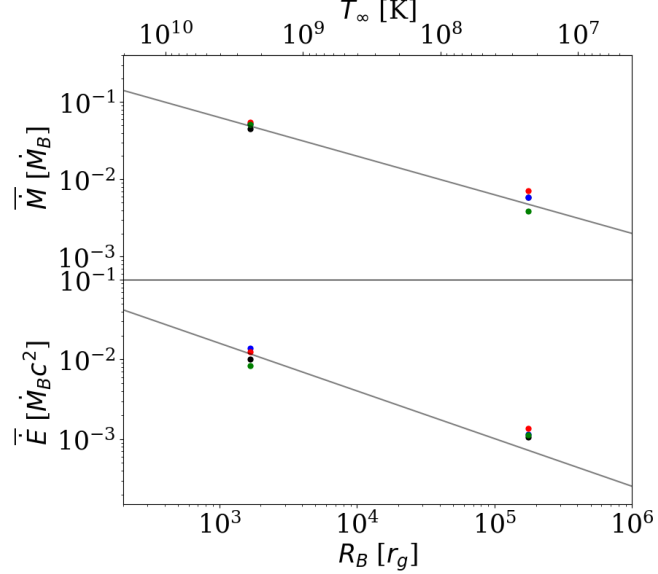


Figure 5. Time-averaged accretion rate \bar{M} and feedback power \bar{E}_{fb} for the $a_* = 0.9$ runs with different ICs: fiducial non-rotating (black), co-rotating (blue), counter-rotating (red), and weakly magnetized (green). For reference, the fitted relations $\bar{M}(R_B, a_* = 0.9)$ and $\bar{E}_{\text{fb}}(R_B, a_* = 0.9)$ (Equations 7 and 8) are shown as black lines.

With the newly adjusted ρh , the function has a value $f(\Gamma_{\max}) < 0$, so there is a unique solution Γ to the equation $f(\Gamma) = 0$. Finally, we recover velocities using the solution.

$$v^i = v_{\parallel}^i + v_{\perp}^i \quad (\text{A7})$$

$$= \frac{S_{\parallel}^i}{\rho h \Gamma^2} + \frac{S_{\perp}^i}{\rho h \Gamma^2 + B^2} \quad (\text{A8})$$

$$= \frac{S_{\parallel}^i}{\rho h \Gamma^2} + \frac{S^i - S_{\parallel}^i}{\rho h \Gamma^2 + B^2}, \quad (\text{A9})$$

where $S_{\parallel}^i = (\vec{B} \cdot \vec{S}) B^i / B^2$.

B. DEPENDENCE ON INITIAL CONDITIONS

Here we demonstrate the robustness of our subgrid prescriptions to different ICs, specifically gas rotation and magnetic field strength. Traditionally, GRMHD simulations distinguish prograde ($a_* > 0$) and retrograde ($a_* < 0$) BH spins and adopt a highly idealized Fishbone & Moncrief (1976)-type torus IC with dynamically subdominant magnetic fields. More recently, however, GRMHD studies have increasingly explored more general classes of ICs and found qualitatively different accretion states (e.g., Ressler et al. 2020, 2021; Lalakos et al. 2022, 2025; Cho et al. 2023, 2024, 2025; Cho & Narayan 2025; Kaaz et al. 2023, 2025; Kwan et al. 2023; Galishnikova et al. 2025; Guo et al. 2025; Chan et al. 2025; Kim & Most 2025).

Among these studies, only a few have reported flips in rotation direction in the presence of strong magnetic fields (Cho et al. 2024, 2025; Cho & Narayan 2025; Galishnikova et al. 2025), challenging the traditional distinction between prograde and retrograde states and instead suggesting that realistic accretion flows may alternate between the two over time. Using the multizone method, Cho et al. (2025) has successfully demonstrated that when evolving Fishbone & Moncrief (1976)-like IC (denoted **T+** and **T-** ICs in their paper) for extended durations with a Bondi radius of $R_B \approx 400 r_g$, the coherent sense of gas rotation is lost as magnetic fields accumulate and become dynamically important. Therefore, the resulting time-averaged feedback efficiency ($\eta \sim 0.3$) differs from that of typical GRMHD simulations, which yield $\eta \sim 1$ for prograde and $\eta \sim 0.1$ for retrograde.

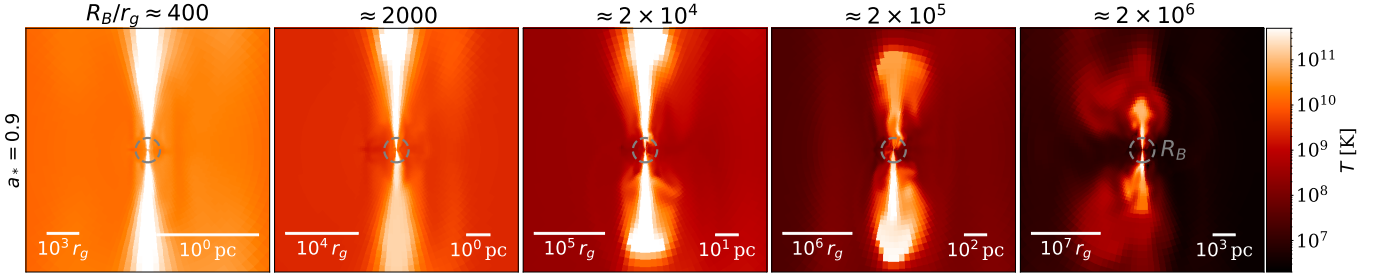


Figure 6. Temperature snapshots of the runs with BH spin $a_* = 0.9$. From left to right, the Bondi radius R_B (shown as gray dotted circles) increases, or equivalently, the asymptotic gas temperature T_∞ decreases. The horizontal bars in the left bottom corner of each panel show scales in gravitational units r_g , while the bars in the right bottom corner show scales in physical units (pc) assuming M87 BH mass.

Here we further demonstrate the independence of the final state on different ICs for even larger Bondi radii of $R_B \approx 2000 r_g$ and $\approx 2 \times 10^5 r_g$. We repeat $a_* = 0.9$ simulations with 3 different types of ICs: prograde, retrograde, and weakly magnetized. Each new ICs differs from the fiducial Bondi-like IC (**B** in Cho et al. 2025) by a single feature. In the prograde and retrograde ICs, the gas co-rotates and counter-rotates with the BH, respectively, with azimuthal velocity $|u^\varphi| = 0.5r^{-3/2}$, respectively. For the weakly magnetized IC, the initial plasma- β is increased from 1 to 100. The three additional large Bondi radius $R_B \approx 2 \times 10^5 r_g$ runs are evolved for $400 t_B$, shorter than the fiducial runtime but still substantial. For reference, the rotational-to-magnetic energy ratio, $\mathcal{R} \equiv \rho r^2 \Omega^2 / b^2$ (Cho & Narayan 2025), measured at R_B is $\mathcal{R} \sim 0.2$ for prograde/retrograde ICs and $\mathcal{R} = 0$ for the fiducial (Bondi-like) and weakly magnetized ICs.

The final time-averages of the accretion rate \bar{M} and feedback power \bar{E}_{fb} are shown in Figure 5. The runs with fiducial Bondi-like ICs are shown as black dots, while the prograde, retrograde, and weakly magnetized IC runs are shown in blue, red, and green, respectively. The three new types of ICs are in good agreement with the fiducial run in both \bar{M} and \bar{E}_{fb} . This confirms our previous finding that the final dynamical equilibrium is insensitive to the initial gas dynamics and magnetic field strengths.

C. DETAILED PROPERTIES OF INDIVIDUAL SIMULATIONS

The detailed accretion and feedback properties of all runs are listed in Table 2. We also present temperature snapshots of the $a_* = 0.9$ runs in Figure 6, taken during their active jet phases. The relativistic jet propagates beyond the Bondi radius R_B , and for the largest Bondi radius, $R_B \approx 2 \times 10^6 r_g$, the jet can extend to kpc scales.

D. LOGNORMAL DISTRIBUTION AND STANDARD ERROR CALCULATION

If X follows a lognormal distribution, then $\ln X$ is normally distributed: $\ln X \sim \mathcal{N}(\mu_{\ln X}, \sigma_{\ln X})$. The mean of X is related to the statistical properties of $\ln X$ as

$$\mu_X = \exp(\mu_{\ln X} + \sigma_{\ln X}^2/2). \quad (\text{D10})$$

The confidence interval of the mean X is

$$\text{CI}(\mu_X) = \exp\left(\mu_{\ln X} + \frac{\sigma_{\ln X}^2}{2} \pm \sqrt{\frac{\sigma_{\ln X}^2}{N_{\text{eff}}} + \frac{\sigma_{\ln X}^4}{2(N_{\text{eff}} - 1)}}\right) \quad (\text{D11})$$

for 68% level confidence (Zhou & Gao 1997; Olsson 2005). Here, N_{eff} is the effective independent sample size. The confidence intervals for each run are shown as errorbars in Figure 1.

Since the time series data $\dot{M}(t)$ and $\eta(t)$ are temporarily correlated, we adopt the effective sample size N_{eff} instead of the total sample size N . We estimate the effective sample size N_{eff} by first taking the autocorrelation of the time series, and dividing N by the autocorrelation length.

REFERENCES

Anglés-Alcázar, D., Quataert, E., Hopkins, P. F., et al. 2021, ApJ, 917, 53, doi: [10.3847/1538-4357/ac09e8](https://doi.org/10.3847/1538-4357/ac09e8)

Anile, A. M. 1990, Relativistic Fluids and Magneto-fluids: With Applications in Astrophysics and Plasma Physics, Cambridge Monographs on Mathematical Physics (Cambridge University Press)

$R_B [r_g]$	BH spin a_*	$N_{V\text{-cycles}}$	Prescription 1 (§ 3.1)		Prescription 2 (§ 3.2)			
			$\bar{M} [\dot{M}_B]$	$\bar{\eta}$	$\mu_{\ln \bar{M}}$	$\sigma_{\ln \bar{M}}$	$\mu_{\ln \eta}$	$\sigma_{\ln \eta}$
≈ 400	0	33	0.12	0.026	-2.2	0.41	-3.8	0.47
	0.1	38	0.16	0.032	-1.9	0.18	-3.5	0.45
	0.3	59	0.11	0.089	-2.3	0.32	-2.5	0.49
	0.5	76	0.11	0.16	-2.2	0.29	-2.0	0.66
	0.7	78	0.091	0.20	-2.5	0.42	-1.8	0.63
	0.9	86	0.090	0.31	-2.5	0.32	-1.4	0.66
≈ 2000	0	15	0.11	0.014	-2.2	0.21	-4.4	0.67
	0.1	15	0.081	0.015	-2.5	0.17	-4.3	0.36
	0.3	24	0.055	0.050	-3.0	0.33	-3.3	0.69
	0.5	50	0.053	0.15	-3.0	0.35	-2.1	0.62
	0.7	44	0.072	0.20	-2.7	0.45	-2.0	0.98
	0.9	48	0.045	0.29	-3.2	0.50	-1.7	1.1
	0.97	50	0.052	0.47	-3.0	0.35	-1.3	1.2
$\approx 2 \times 10^4$	0	45	0.041	0.016	-3.4	0.60	-4.3	0.52
	0.1	46	0.056	0.018	-3.0	0.35	-4.2	0.59
	0.3	65	0.033	0.039	-3.6	0.64	-3.5	0.70
	0.5	105	0.028	0.11	-3.7	0.48	-2.7	0.95
	0.7	138	0.030	0.16	-3.6	0.53	-2.4	1.1
	0.9	124	0.022	0.36	-4.0	0.73	-2.0	1.5
$\approx 2 \times 10^5$	0	105	0.017	0.013	-4.5	-0.99	-4.6	0.64
	0.1	109	0.016	0.014	-4.5	0.78	-4.5	0.70
	0.3	156	0.014	0.031	-4.6	0.83	-3.8	0.84
	0.5	181	0.011	0.067	-4.9	0.91	-3.4	1.1
	0.7	258	0.0071	0.16	-5.4	0.93	-2.6	1.3
	0.9	262	0.0059	0.31	-5.6	1.0	-2.1	1.5
$\approx 2 \times 10^6$	0	164	0.0036	0.013	-6.3	1.6	-4.6	0.80
	0.1	210	0.0034	0.0095	-6.3	1.3	-5.0	0.99
	0.3	224	0.0027	0.026	-6.6	1.3	-4.2	1.1
	0.5	322	0.0021	0.043	-7.0	1.6	-3.8	1.2
	0.7	519	0.0013	0.18	-7.2	1.3	-2.8	1.5
	0.9	523	0.00092	0.26	-7.8	1.4	-2.5	1.6

Table 2. Detailed information on BH accretion and feedback for all simulations. The first three columns list the Bondi radius R_B , BH spin a_* , and the total number of V-cycles. Columns 4 and 5 give time-averaged accretion rate \bar{M} and the feedback efficiency $\bar{\eta}$ in Section 3.1. The last four columns show the mean μ and standard deviation σ of $\ln(\bar{M}/\dot{M}_B)$ and $\ln \eta$ relevant to Section 3.2.

Baganoff, F. K., Maeda, Y., Morris, M., et al. 2003, ApJ, 591, 891, doi: [10.1086/375145](https://doi.org/10.1086/375145)

Beckmann, R. S., Dubois, Y., Volonteri, M., et al. 2025, MNRAS, 536, 1838, doi: [10.1093/mnras/stae2595](https://doi.org/10.1093/mnras/stae2595)

Bisnovatyi-Kogan, G. S., & Ruzmaikin, A. A. 1974, Ap&SS, 28, 45, doi: [10.1007/BF00642237](https://doi.org/10.1007/BF00642237)

—. 1976, Ap&SS, 42, 401, doi: [10.1007/BF01225967](https://doi.org/10.1007/BF01225967)

Blandford, R. D., & Znajek, R. L. 1977, MNRAS, 179, 433, doi: [10.1093/mnras/179.3.433](https://doi.org/10.1093/mnras/179.3.433)

Bondi, H. 1952, MNRAS, 112, 195, doi: [10.1093/mnras/112.2.195](https://doi.org/10.1093/mnras/112.2.195)

Chan, H.-S., Dhang, P., Dexter, J., & Begelman, M. C. 2025, ApJ, 985, 135, doi: [10.3847/1538-4357/adce7f](https://doi.org/10.3847/1538-4357/adce7f)

Cho, H., & Narayan, R. 2022, ApJ, 932, 97, doi: [10.3847/1538-4357/ac6d5c](https://doi.org/10.3847/1538-4357/ac6d5c)

—. 2025, arXiv e-prints, arXiv:2507.13441, <https://arxiv.org/abs/2507.13441>

Cho, H., Prather, B. S., Narayan, R., et al. 2023, ApJL, 959, L22, doi: [10.3847/2041-8213/ad1048](https://doi.org/10.3847/2041-8213/ad1048)

Cho, H., Prather, B. S., Narayan, R., Su, K.-Y., & Natarajan, P. 2025, ApJ, 995, 122, doi: [10.3847/1538-4357/ae1fdb](https://doi.org/10.3847/1538-4357/ae1fdb)

Cho, H., Prather, B. S., Su, K.-Y., Narayan, R., & Natarajan, P. 2024, *ApJ*, 977, 200, doi: [10.3847/1538-4357/ad9561](https://doi.org/10.3847/1538-4357/ad9561)

Davé, R., Anglés-Alcázar, D., Narayanan, D., et al. 2019, *MNRAS*, 486, 2827, doi: [10.1093/mnras/stz937](https://doi.org/10.1093/mnras/stz937)

Di Matteo, T., Allen, S. W., Fabian, A. C., Wilson, A. S., & Young, A. J. 2003, *ApJ*, 582, 133, doi: [10.1086/344504](https://doi.org/10.1086/344504)

Dubois, Y., Beckmann, R., Bournaud, F., et al. 2021, *A&A*, 651, A109, doi: [10.1051/0004-6361/202039429](https://doi.org/10.1051/0004-6361/202039429)

EHT MWL Science Working Group, Algaba, J. C., Anczarski, J., et al. 2021, *ApJL*, 911, L11, doi: [10.3847/2041-8213/abef71](https://doi.org/10.3847/2041-8213/abef71)

Fishbone, L. G., & Moncrief, V. 1976, *ApJ*, 207, 962, doi: [10.1086/154565](https://doi.org/10.1086/154565)

Galishnikova, A., Philippov, A., Quataert, E., Chatterjee, K., & Liska, M. 2025, *ApJ*, 978, 148, doi: [10.3847/1538-4357/ad9926](https://doi.org/10.3847/1538-4357/ad9926)

Gammie, C. F., McKinney, J. C., & Tóth, G. 2003, *ApJ*, 589, 444, doi: [10.1086/374594](https://doi.org/10.1086/374594)

Gammie, C. F., Shapiro, S. L., & McKinney, J. C. 2004, *ApJ*, 602, 312, doi: [10.1086/380996](https://doi.org/10.1086/380996)

Guo, M., Stone, J. M., Kim, C.-G., & Quataert, E. 2023, *ApJ*, 946, 26, doi: [10.3847/1538-4357/acb81e](https://doi.org/10.3847/1538-4357/acb81e)

Guo, M., Stone, J. M., Quataert, E., & Kim, C.-G. 2024, *ApJ*, 973, 141, doi: [10.3847/1538-4357/ad5fe7](https://doi.org/10.3847/1538-4357/ad5fe7)

Guo, M., Stone, J. M., Quataert, E., & Springel, V. 2025, *ApJ*, 987, 202, doi: [10.3847/1538-4357/add1da](https://doi.org/10.3847/1538-4357/add1da)

Habouzit, M., Somerville, R. S., Li, Y., et al. 2022, *MNRAS*, 509, 3015, doi: [10.1093/mnras/stab3147](https://doi.org/10.1093/mnras/stab3147)

Haidar, H., Habouzit, M., Volonteri, M., et al. 2022, *MNRAS*, 514, 4912, doi: [10.1093/mnras/stac1659](https://doi.org/10.1093/mnras/stac1659)

Heckman, T. M., & Best, P. N. 2014, *ARA&A*, 52, 589, doi: [10.1146/annurev-astro-081913-035722](https://doi.org/10.1146/annurev-astro-081913-035722)

Hopkins, P. F., & Most, E. R. 2025, arXiv e-prints, arXiv:2510.09756, doi: [10.48550/arXiv.2510.09756](https://doi.org/10.48550/arXiv.2510.09756)

Hopkins, P. F., & Quataert, E. 2010, *MNRAS*, 407, 1529, doi: [10.1111/j.1365-2966.2010.17064.x](https://doi.org/10.1111/j.1365-2966.2010.17064.x)

Hopkins, P. F., Grudic, M. Y., Su, K.-Y., et al. 2024a, *The Open Journal of Astrophysics*, 7, 18, doi: [10.21105/astro.2309.13115](https://doi.org/10.21105/astro.2309.13115)

Hopkins, P. F., Squire, J., Su, K.-Y., et al. 2024b, *The Open Journal of Astrophysics*, 7, 19, doi: [10.21105/astro.2310.04506](https://doi.org/10.21105/astro.2310.04506)

Hopkins, P. F., Su, K.-Y., Murray, N., et al. 2025, *The Open Journal of Astrophysics*, 8, 48, doi: [10.33232/001c.137296](https://doi.org/10.33232/001c.137296)

Huško, F., Lacey, C. G., Schaye, J., et al. 2025, arXiv e-prints, arXiv:2509.05179, doi: [10.48550/arXiv.2509.05179](https://doi.org/10.48550/arXiv.2509.05179)

Igumenshchev, I. V., Narayan, R., & Abramowicz, M. A. 2003, *ApJ*, 592, 1042, doi: [10.1086/375769](https://doi.org/10.1086/375769)

Kaaz, N., Liska, M., Tchekhovskoy, A., Hopkins, P. F., & Jacquemin-Ide, J. 2025, *ApJ*, 979, 248, doi: [10.3847/1538-4357/ad9a86](https://doi.org/10.3847/1538-4357/ad9a86)

Kaaz, N., Murguia-Berthier, A., Chatterjee, K., Liska, M. T. P., & Tchekhovskoy, A. 2023, *ApJ*, 950, 31, doi: [10.3847/1538-4357/acc7a1](https://doi.org/10.3847/1538-4357/acc7a1)

Kastaun, W., Kalinani, J. V., & Ciolfi, R. 2021, *PhRvD*, 103, 023018, doi: [10.1103/PhysRevD.103.023018](https://doi.org/10.1103/PhysRevD.103.023018)

Kim, Y., & Most, E. R. 2025, *PhRvD*, 111, 083025, doi: [10.1103/PhysRevD.111.083025](https://doi.org/10.1103/PhysRevD.111.083025)

Komissarov, S. S. 1999, *MNRAS*, 303, 343, doi: [10.1046/j.1365-8711.1999.02244.x](https://doi.org/10.1046/j.1365-8711.1999.02244.x)

—. 2009, *Journal of Korean Physical Society*, 54, 2503, doi: [10.3938/jkps.54.2503](https://doi.org/10.3938/jkps.54.2503)

Kormendy, J., & Ho, L. C. 2013, *ARA&A*, 51, 511, doi: [10.1146/annurev-astro-082708-101811](https://doi.org/10.1146/annurev-astro-082708-101811)

Kwan, T. M., Dai, L., & Tchekhovskoy, A. 2023, *ApJL*, 946, L42, doi: [10.3847/2041-8213/acc334](https://doi.org/10.3847/2041-8213/acc334)

Lalakos, A., Tchekhovskoy, A., Bromberg, O., et al. 2024, *ApJ*, 964, 79, doi: [10.3847/1538-4357/ad0974](https://doi.org/10.3847/1538-4357/ad0974)

Lalakos, A., Tchekhovskoy, A., Most, E. R., et al. 2025, arXiv e-prints, arXiv:2505.23888, doi: [10.48550/arXiv.2505.23888](https://doi.org/10.48550/arXiv.2505.23888)

Lalakos, A., Gottlieb, O., Kaaz, N., et al. 2022, *ApJL*, 936, L5, doi: [10.3847/2041-8213/ac7bed](https://doi.org/10.3847/2041-8213/ac7bed)

Lasota, J.-P., Gourgoulhon, E., Abramowicz, M., Tchekhovskoy, A., & Narayan, R. 2014, *PhRvD*, 89, 024041, doi: [10.1103/PhysRevD.89.024041](https://doi.org/10.1103/PhysRevD.89.024041)

Liska, M., Tchekhovskoy, A., & Quataert, E. 2020, *MNRAS*, 494, 3656, doi: [10.1093/mnras/staa955](https://doi.org/10.1093/mnras/staa955)

Liska, M. T. P., Chatterjee, K., Issa, D., et al. 2022, *ApJS*, 263, 26, doi: [10.3847/1538-4365/ac9966](https://doi.org/10.3847/1538-4365/ac9966)

Lowell, B., Jacquemin-Ide, J., Tchekhovskoy, A., & Duncan, A. 2024, *ApJ*, 960, 82, doi: [10.3847/1538-4357/ad09af](https://doi.org/10.3847/1538-4357/ad09af)

Lu, R.-S., Asada, K., Krichbaum, T. P., et al. 2023, *Nature*, 616, 686, doi: [10.1038/s41586-023-05843-w](https://doi.org/10.1038/s41586-023-05843-w)

McKinney, J. C., Tchekhovskoy, A., & Blandford, R. D. 2012, *MNRAS*, 423, 3083, doi: [10.1111/j.1365-2966.2012.21074.x](https://doi.org/10.1111/j.1365-2966.2012.21074.x)

Michel, F. C. 1972, *Ap&SS*, 15, 153, doi: [10.1007/BF00649949](https://doi.org/10.1007/BF00649949)

Mignone, A., & McKinney, J. C. 2007, *MNRAS*, 378, 1118, doi: [10.1111/j.1365-2966.2007.11849.x](https://doi.org/10.1111/j.1365-2966.2007.11849.x)

Narayan, R., Chael, A., Chatterjee, K., Ricarte, A., & Curd, B. 2022, *MNRAS*, 511, 3795, doi: [10.1093/mnras/stac285](https://doi.org/10.1093/mnras/stac285)

Narayan, R., Igumenshchev, I. V., & Abramowicz, M. A. 2003, *PASJ*, 55, L69, doi: [10.1093/pasj/55.6.L69](https://doi.org/10.1093/pasj/55.6.L69)

Narayan, R., & Yi, I. 1994, ApJL, 428, L13, doi: [10.1086/187381](https://doi.org/10.1086/187381)

Natarajan, P. 2011, arXiv e-prints, arXiv:1105.4902, doi: [10.48550/arXiv.1105.4902](https://doi.org/10.48550/arXiv.1105.4902)

Ni, Y., Di Matteo, T., Bird, S., et al. 2022, MNRAS, 513, 670, doi: [10.1093/mnras/stac351](https://doi.org/10.1093/mnras/stac351)

Noble, S. C., Gammie, C. F., McKinney, J. C., & Del Zanna, L. 2006, ApJ, 641, 626, doi: [10.1086/500349](https://doi.org/10.1086/500349)

Novikov, I. D., & Thorne, K. S. 1973, in Black Holes (Les Astres Occlus), ed. C. DeWitt & B. S. DeWitt, 343–450

Olsson, U. 2005, Journal of Statistics Education, 13, doi: [10.1080/10691898.2005.11910638](https://doi.org/10.1080/10691898.2005.11910638)

Ott, J., Walter, F., & Brinks, E. 2005, MNRAS, 358, 1423, doi: [10.1111/j.1365-2966.2005.08862.x](https://doi.org/10.1111/j.1365-2966.2005.08862.x)

Owen, F. N., Eilek, J. A., & Kassim, N. E. 2000, ApJ, 543, 611, doi: [10.1086/317151](https://doi.org/10.1086/317151)

Penrose, R. 1969, Nuovo Cimento Rivista Serie, 1, 252

Porras-Valverde, A. J., Natarajan, P., Ricarte, A., et al. 2025, arXiv e-prints, arXiv:2511.08683, doi: [10.48550/arXiv.2511.08683](https://doi.org/10.48550/arXiv.2511.08683)

Porth, O., Chatterjee, K., Narayan, R., et al. 2019, ApJS, 243, 26, doi: [10.3847/1538-4365/ab29fd](https://doi.org/10.3847/1538-4365/ab29fd)

Prather, B. S. 2024, arXiv e-prints, arXiv:2408.01361, doi: [10.48550/arXiv.2408.01361](https://doi.org/10.48550/arXiv.2408.01361)

Ressler, S. M., Quataert, E., White, C. J., & Blaes, O. 2021, MNRAS, 504, 6076, doi: [10.1093/mnras/stab311](https://doi.org/10.1093/mnras/stab311)

Ressler, S. M., White, C. J., Quataert, E., & Stone, J. M. 2020, ApJL, 896, L6, doi: [10.3847/2041-8213/ab9532](https://doi.org/10.3847/2041-8213/ab9532)

Ricarte, A., Narayan, R., & Curd, B. 2023, ApJL, 954, L22, doi: [10.3847/2041-8213/aceda5](https://doi.org/10.3847/2041-8213/aceda5)

Russell, H. R., Fabian, A. C., McNamara, B. R., & Broderick, A. E. 2015, MNRAS, 451, 588, doi: [10.1093/mnras/stv954](https://doi.org/10.1093/mnras/stv954)

Schaye, J., Chaikin, E., Schaller, M., et al. 2025, arXiv e-prints, arXiv:2508.21126, doi: [10.48550/arXiv.2508.21126](https://doi.org/10.48550/arXiv.2508.21126)

Shakura, N. I., & Sunyaev, R. A. 1973, A&A, 24, 337

Shapiro, S. L. 2005, ApJ, 620, 59, doi: [10.1086/427065](https://doi.org/10.1086/427065)

Shapiro, S. L., & Teukolsky, S. A. 1983, Black holes, white dwarfs, and neutron stars : the physics of compact objects

Singh, A., Bégué, D., & Pe'er, A. 2025, ApJL, 981, L11, doi: [10.3847/2041-8213/adb749](https://doi.org/10.3847/2041-8213/adb749)

Sądowski, A., Narayan, R., Tchekhovskoy, A., & Zhu, Y. 2013, MNRAS, 429, 3533, doi: [10.1093/mnras/sts632](https://doi.org/10.1093/mnras/sts632)

Su, K.-Y., Natarajan, P., Cho, H., et al. 2025a, ApJL, 981, L33, doi: [10.3847/2041-8213/adb7dd](https://doi.org/10.3847/2041-8213/adb7dd)

Su, K.-Y., Ricarte, A., Natarajan, P., et al. 2025b, arXiv e-prints, arXiv:2511.08668, doi: [10.48550/arXiv.2511.08668](https://doi.org/10.48550/arXiv.2511.08668)

Talbot, R. Y., Bourne, M. A., & Sijacki, D. 2021, MNRAS, 504, 3619, doi: [10.1093/mnras/stab804](https://doi.org/10.1093/mnras/stab804)

Tchekhovskoy, A., McKinney, J. C., & Narayan, R. 2012, in Journal of Physics Conference Series, Vol. 372, Journal of Physics Conference Series (IOP), 012040, doi: [10.1088/1742-6596/372/1/012040](https://doi.org/10.1088/1742-6596/372/1/012040)

Tchekhovskoy, A., Narayan, R., & McKinney, J. C. 2010, ApJ, 711, 50, doi: [10.1088/0004-637X/711/1/50](https://doi.org/10.1088/0004-637X/711/1/50)

—. 2011, MNRAS, 418, L79, doi: [10.1111/j.1745-3933.2011.01147.x](https://doi.org/10.1111/j.1745-3933.2011.01147.x)

Tremmel, M., Karcher, M., Governato, F., et al. 2017, MNRAS, 470, 1121, doi: [10.1093/mnras/stx1160](https://doi.org/10.1093/mnras/stx1160)

Vikhlinin, A., Markevitch, M., Murray, S. S., et al. 2005, ApJ, 628, 655, doi: [10.1086/431142](https://doi.org/10.1086/431142)

Wallbank, A. N., Maughan, B. J., Gastaldello, F., Potter, C., & Wik, D. R. 2022, MNRAS, 517, 5594, doi: [10.1093/mnras/stac3055](https://doi.org/10.1093/mnras/stac3055)

Weinberger, R., Springel, V., Pakmor, R., et al. 2018, MNRAS, 479, 4056, doi: [10.1093/mnras/sty1733](https://doi.org/10.1093/mnras/sty1733)

Weinberger, R., Su, K.-Y., Ehlert, K., et al. 2023, MNRAS, 523, 1104, doi: [10.1093/mnras/stad1396](https://doi.org/10.1093/mnras/stad1396)

Wellons, S., Faucher-Giguère, C.-A., Hopkins, P. F., et al. 2023, MNRAS, 520, 5394, doi: [10.1093/mnras/stad511](https://doi.org/10.1093/mnras/stad511)

White, C. J., Stone, J. M., & Gammie, C. F. 2016, ApJS, 225, 22, doi: [10.3847/0067-0049/225/2/22](https://doi.org/10.3847/0067-0049/225/2/22)

Yuan, F., & Narayan, R. 2014, ARA&A, 52, 529, doi: [10.1146/annurev-astro-082812-141003](https://doi.org/10.1146/annurev-astro-082812-141003)

Zhou, X.-H., & Gao, S. 1997, Statistics in Medicine, 16, 783, doi: [10.1002/\(SICI\)1097-0258\(19970415\)16:7<783::AID-SIM488>3.0.CO;2-2](https://doi.org/10.1002/(SICI)1097-0258(19970415)16:7<783::AID-SIM488>3.0.CO;2-2)